Journal of Geophysical Research Atmospheres

Supporting Information for

Anthropogenic Aerosol Indirect Effects in Cirrus Clouds

Joyce E. Penner[1], Cheng Zhou[1], Anne Garnier[2,3], David L. Mitchell[4]

[1]Department of Climate and Sace Sciences and Engineering, University of Michigan, Ann Arbor, MI, USA, [2]Science Systems and Applications, Inc., Hampton, VA, USA, [3]NASA Langley Research Center, Hampton, VA, USA, [4]Desert Research Institute, Reno, NV, USA

Contents of this file

Formulas associated with Podglajen et al. (2016) parameterization, Figures S1 to S12, Tables S1 and S2

Introduction

This supporting information provides additional explanations and plots and tables referenced in the paper which are not central to the conclusions of the paper.

Formulas associated with the gravity wave spectrum

At the equator for an altitude of 19 km, the vertical velocity *w* is determined from a Laplace (or double exponential) distribution with a standard deviation of 0.17 m s^{-1}:

$$W = -b\, sgn(U) \ln(1 - 2|U|)$$

Where *U* is a random variable from the uniform distribution in the interval [-0.5,0.5] and b=0.1202 ($\sqrt{2}b$ is the standard deviation of *W*). Values of *W* are constant for a time interval of 2.2 minutes. The final interval within the 30 minute time step of the CAM model is curtailed to less than 30 minutes.

For other altitudes, the standard deviation in the Laplace distribution formula is scaled by Brunt-Väisälä frequency and atmospheric density following Eqn. 12 in the supplemental material of Podglajen et al. (2016). For other latitudes, seasons and

topography, we further scale the standard deviation in the Laplace distribution by the mesoscale fluctuation amplitudes (MFA) calculated following Eqn. 4 and 5 in Gary (2008).

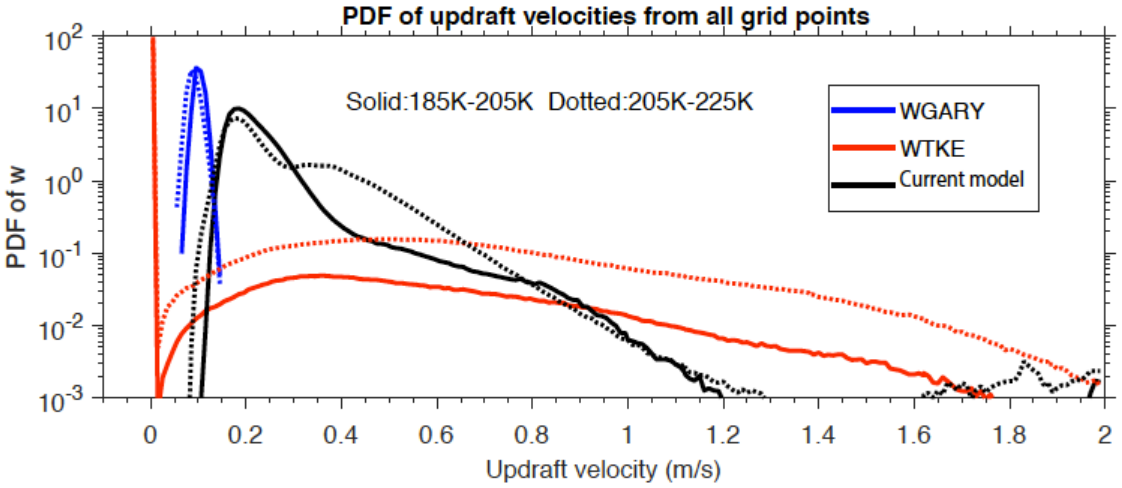

Figure S1. The probability distribution frequency of updraft velocities over all grid points in the range from 185K - 205K and from 205K – 225K. WTKE refers to the sub-trid scale updrafts determine in the standard CAM formulation based on turbulent kinetic energy. WGARY are the sug-grid scale updraft used by Wang & Penner (2010) and Wang et al. (2014), which are based on Gary (2006; 2008). The plot from the current model is the pdf of the standard deviation of the reconstructed vertical velocity wave series. The vertical velocity itself can be positive or negative, but the standard deviation is always positive.

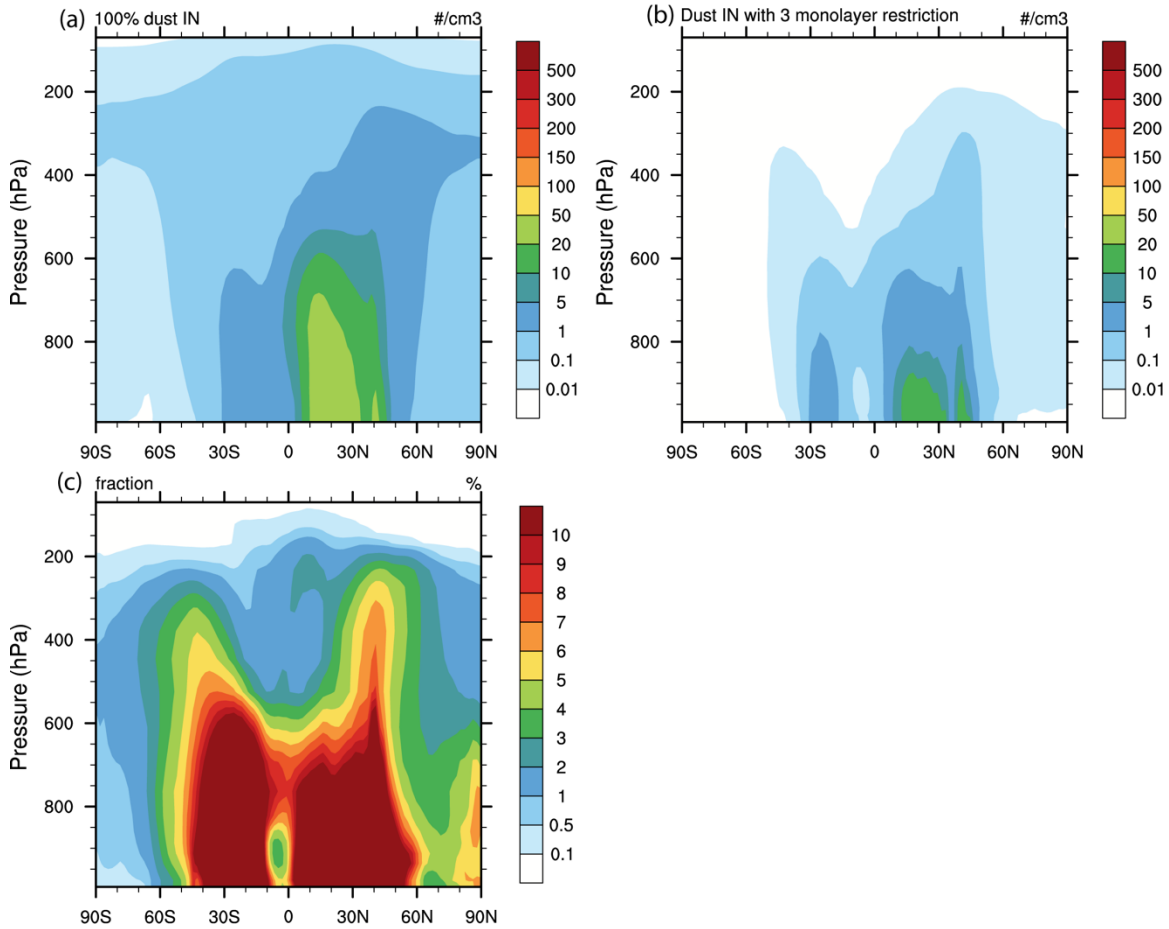

Figure S2. (a) The zonal average total number concentration of dust particles (cm^{-3}) calculated in the model, (b) the number concentration of dust particles with < 3 monolayers of sulfate, and (c) the fraction of dust particles with < 3 monolayers of sulfate.

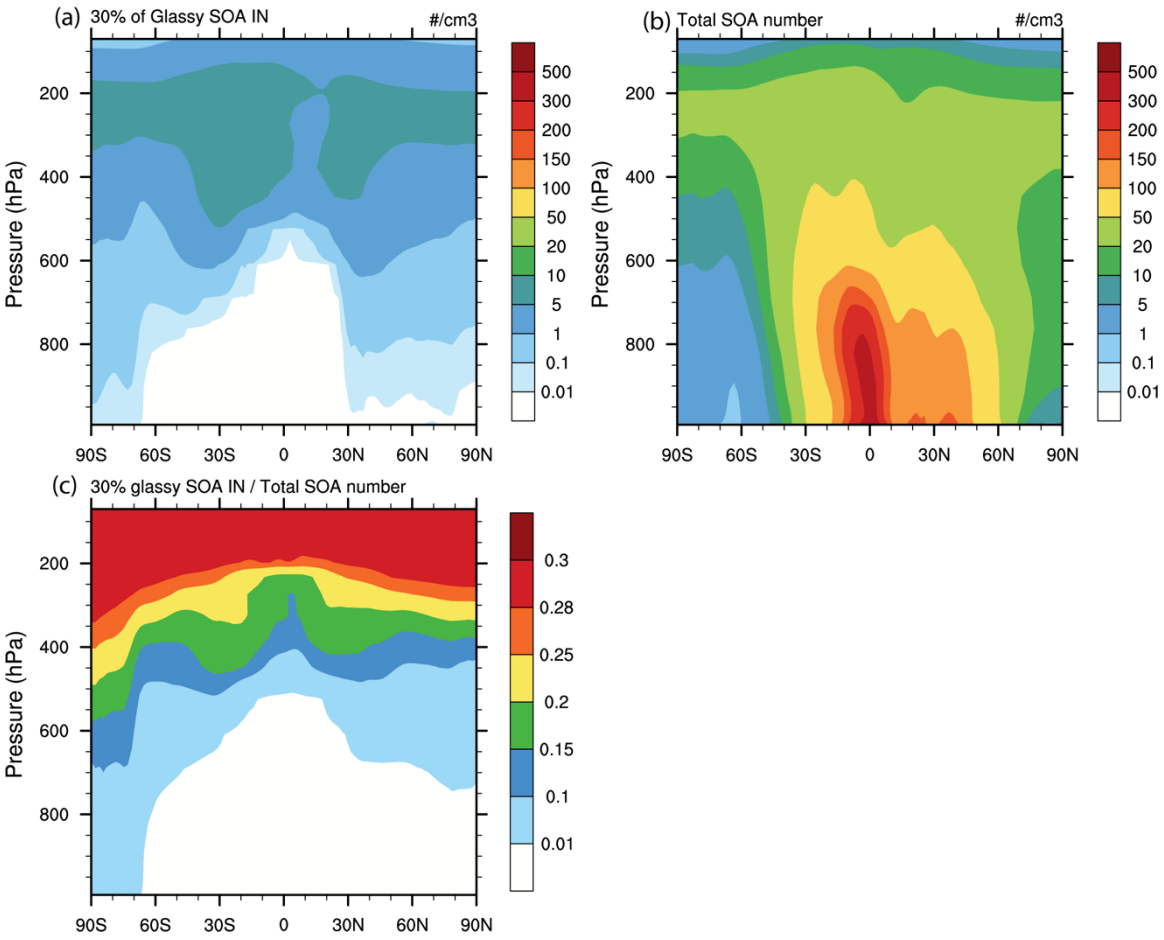

Figure S3. (a) The zonal average calculated number concentration of SOA particles (cm^{-3}) that satisfy the glassy SOA criterion based on Wang et al. (2012) when restricted to < 30% of the total SOA, (b) the total number concentration of SOA particles, and (c) the fraction of SOA particles that are considered glassy in the model.

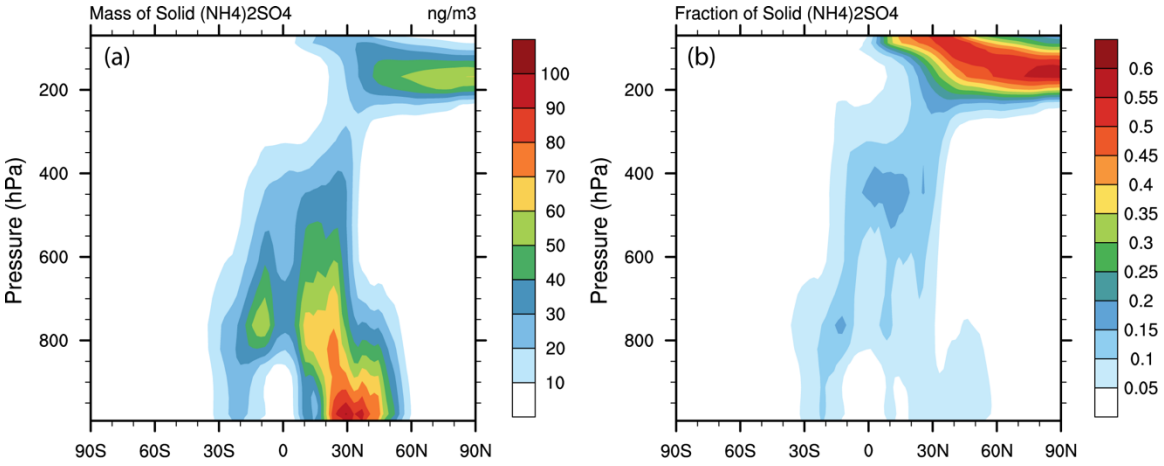

Figure S4. (a) The zonal average mass concentration of crystalline $(NH_4)_2SO_4$ calculated in the model and (b) the fraction of the total $(NH_4)_2SO_4$ that is calculated to be crystalline and thus available to act as an INP.

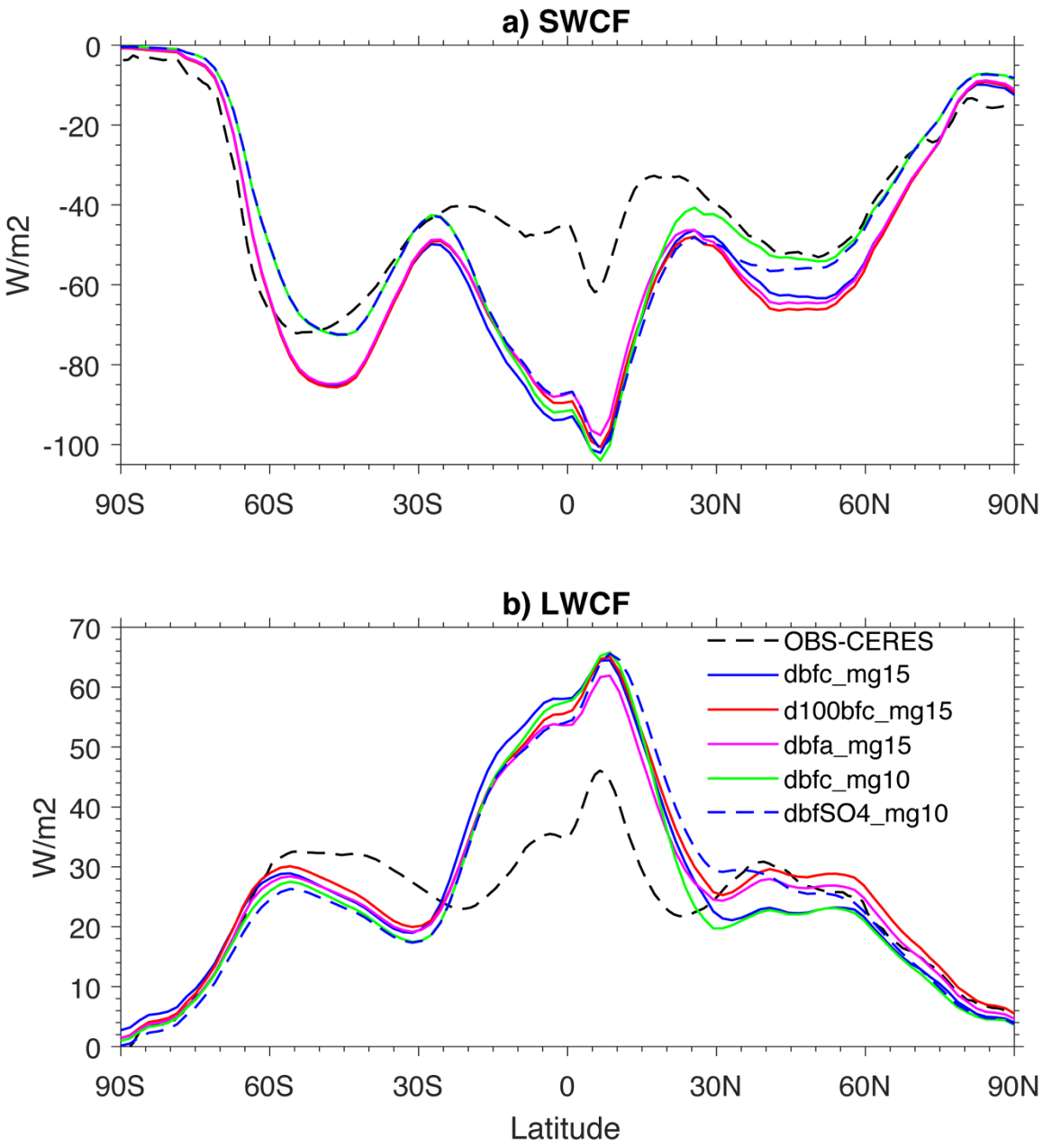

Figure S5. Short wave cloud forcing versus latitude for the CERES observations (Loeb et al., 2009) and several simulations.

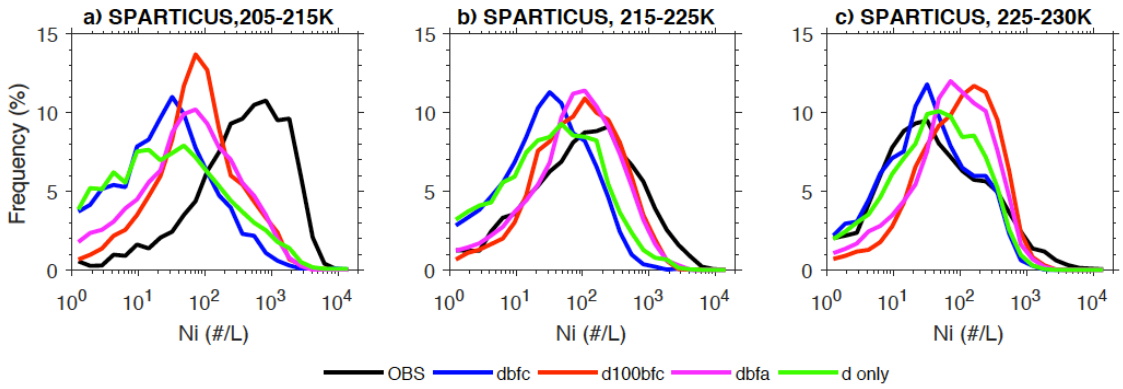

Figure S6. The frequency distribution of ice crystal number concentrations in different temperature ranges from the DBFC, d100bfc, and dbfa simulations (see Table 1) A simulation including only dust with less than 3 monolayers of sulfate as an INP is also included. The observations are from the SPARTICUS field campaign (Zhang et al., 2013) over the ARM SGP site.

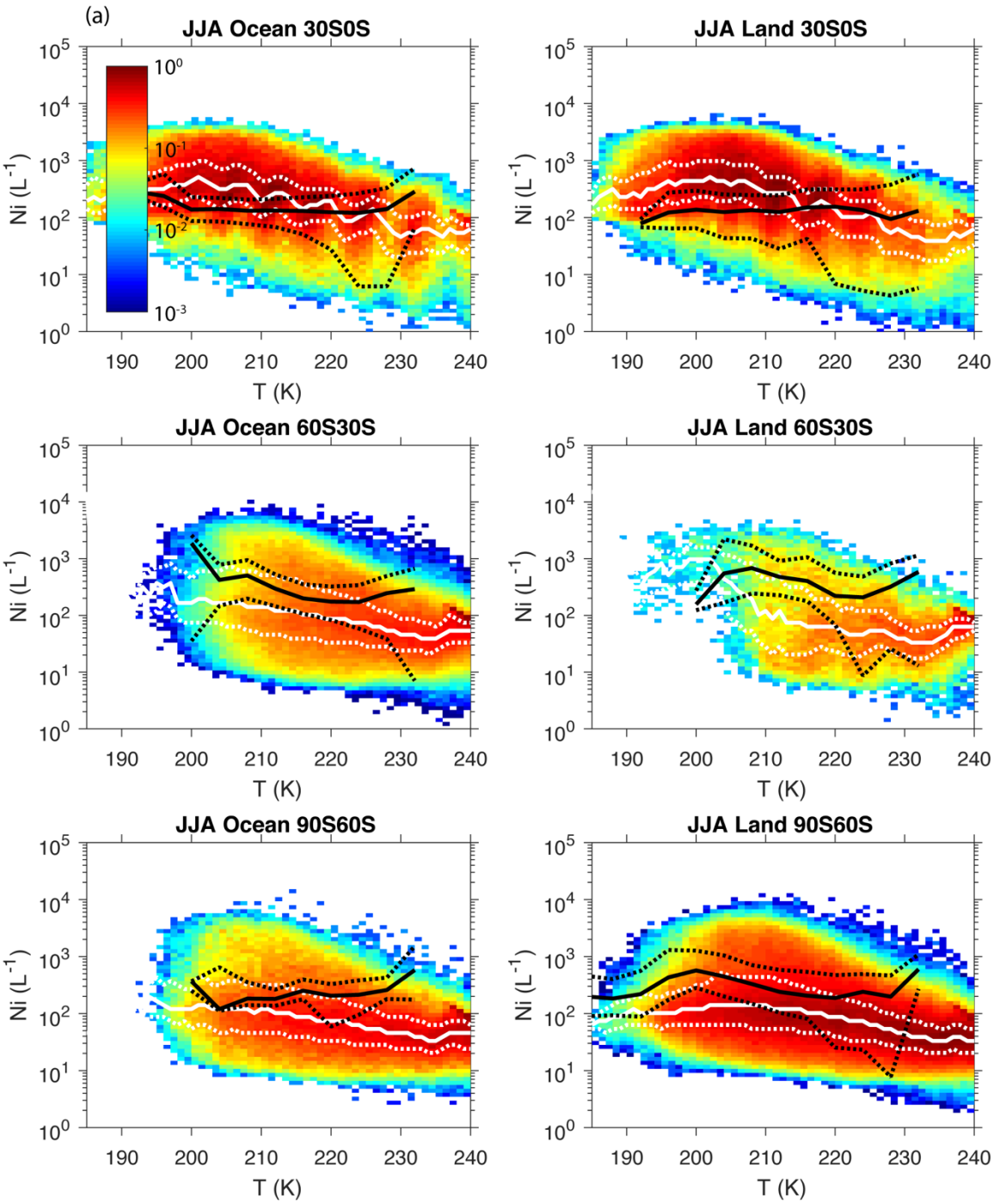
(a)
JJA Ocean 30S0S
JJA Land 30S0S
JJA Ocean 60S30S
JJA Land 60S30S
JJA Ocean 90S60S
JJA Land 90S60S
Ni (L^{-1})
T (K)
10^{0}
10^{-1}
10^{-2}
10^{-3}

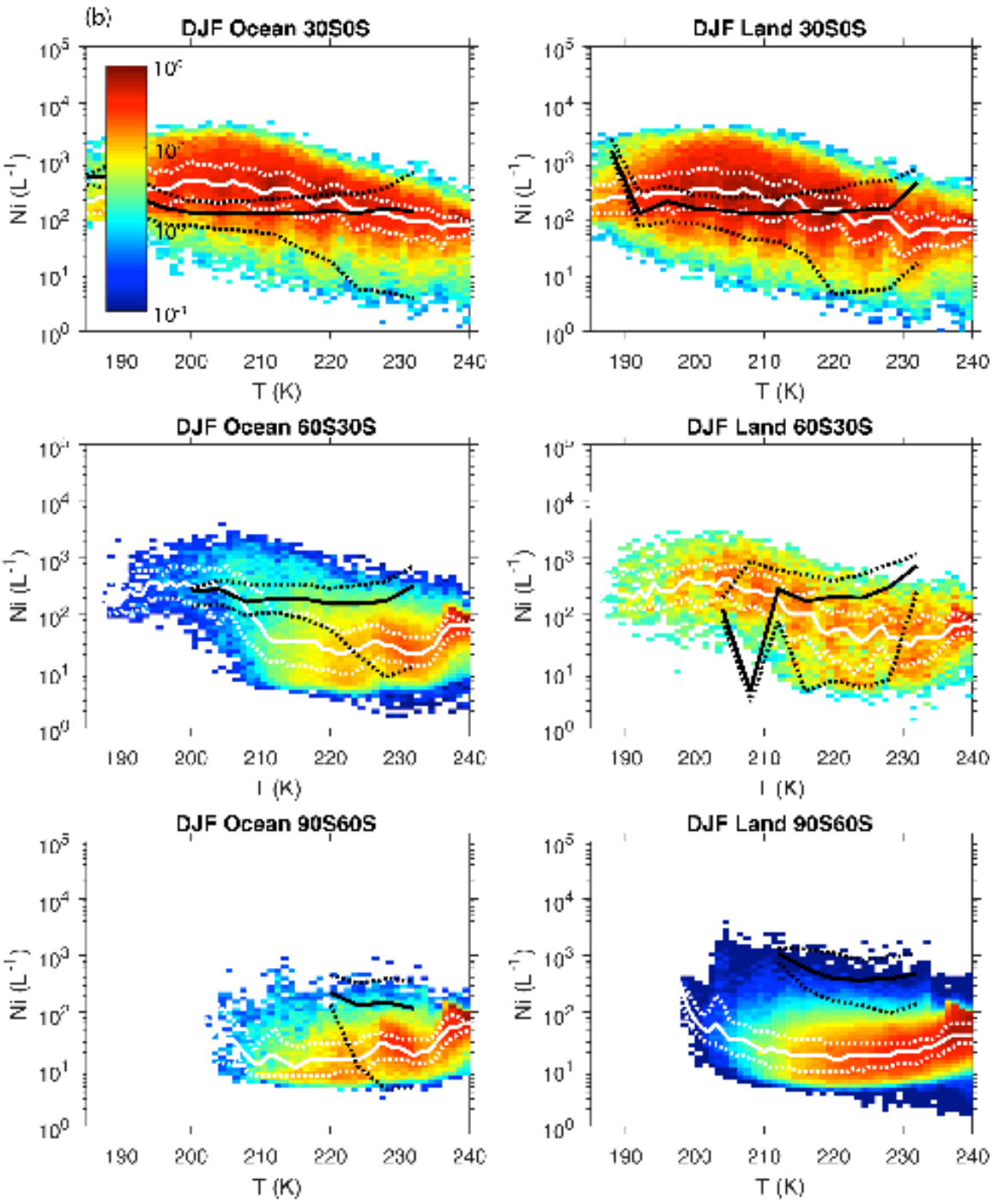

Figure S7. (a) In-cloud ice number concentrations from the $N(D)_1$=0 assumption for CALIPSO observations summarized by Mitchell et al. (2018) together with the dfbc simulation for JJA in the Southern Hemisphere. The black full and dotted lines show the median, 25th percentile and 75th percentile values of the observations, while the white lines as well as the color contours show the simulations. The modeled cloud optical depth is restricted to the range from 0.3 to 3.0. (b) as in (a) for DJF in the Southern Hemisphere.

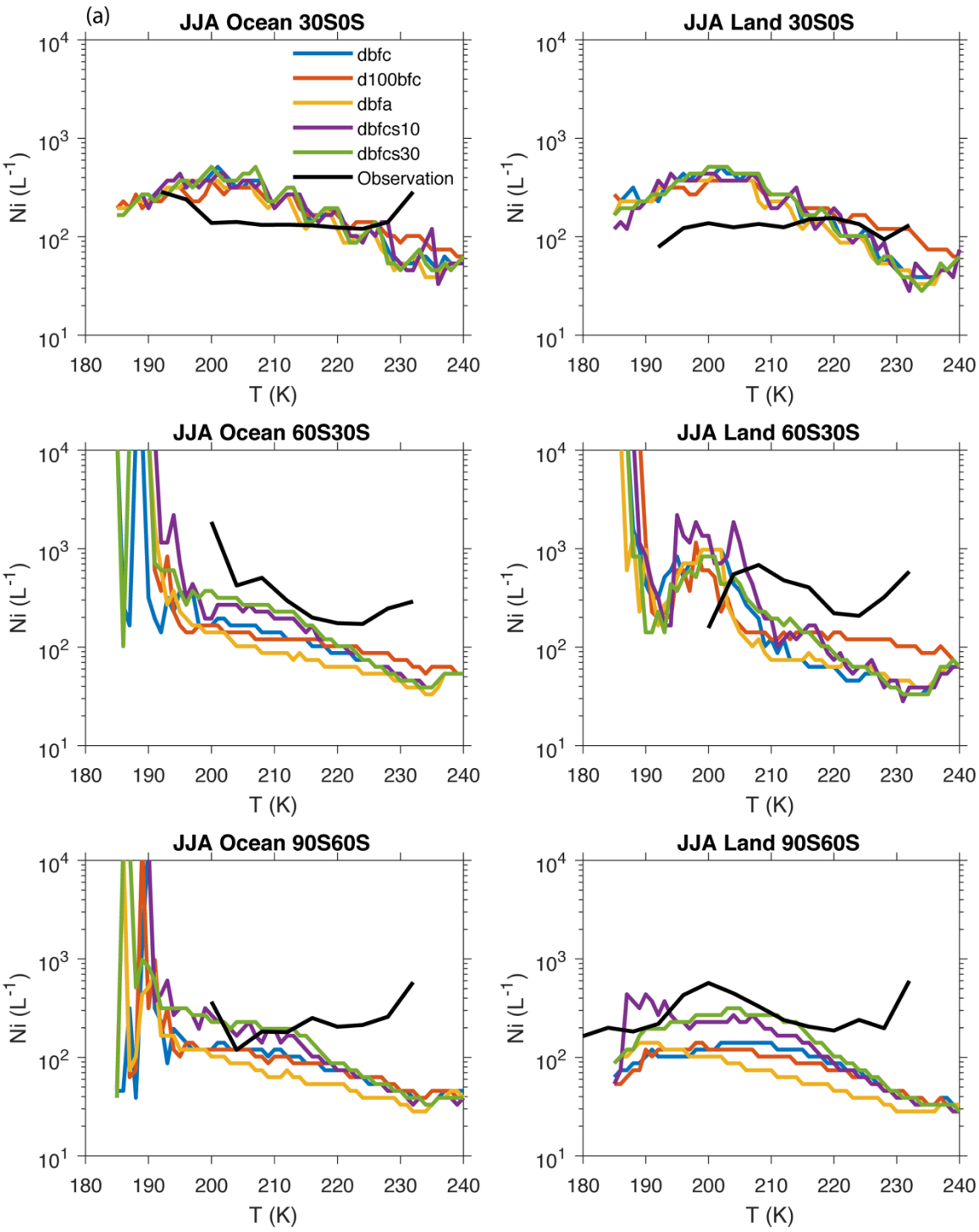
(a)
JJA Ocean 30S0S
JJA Land 30S0S
JJA Ocean 60S30S
JJA Land 60S30S
JJA Ocean 90S60S
JJA Land 90S60S
dbfc
d100bfc
dbfa
dbfcs10
dbfcs30
Observation
Ni (L-1)
T (K)

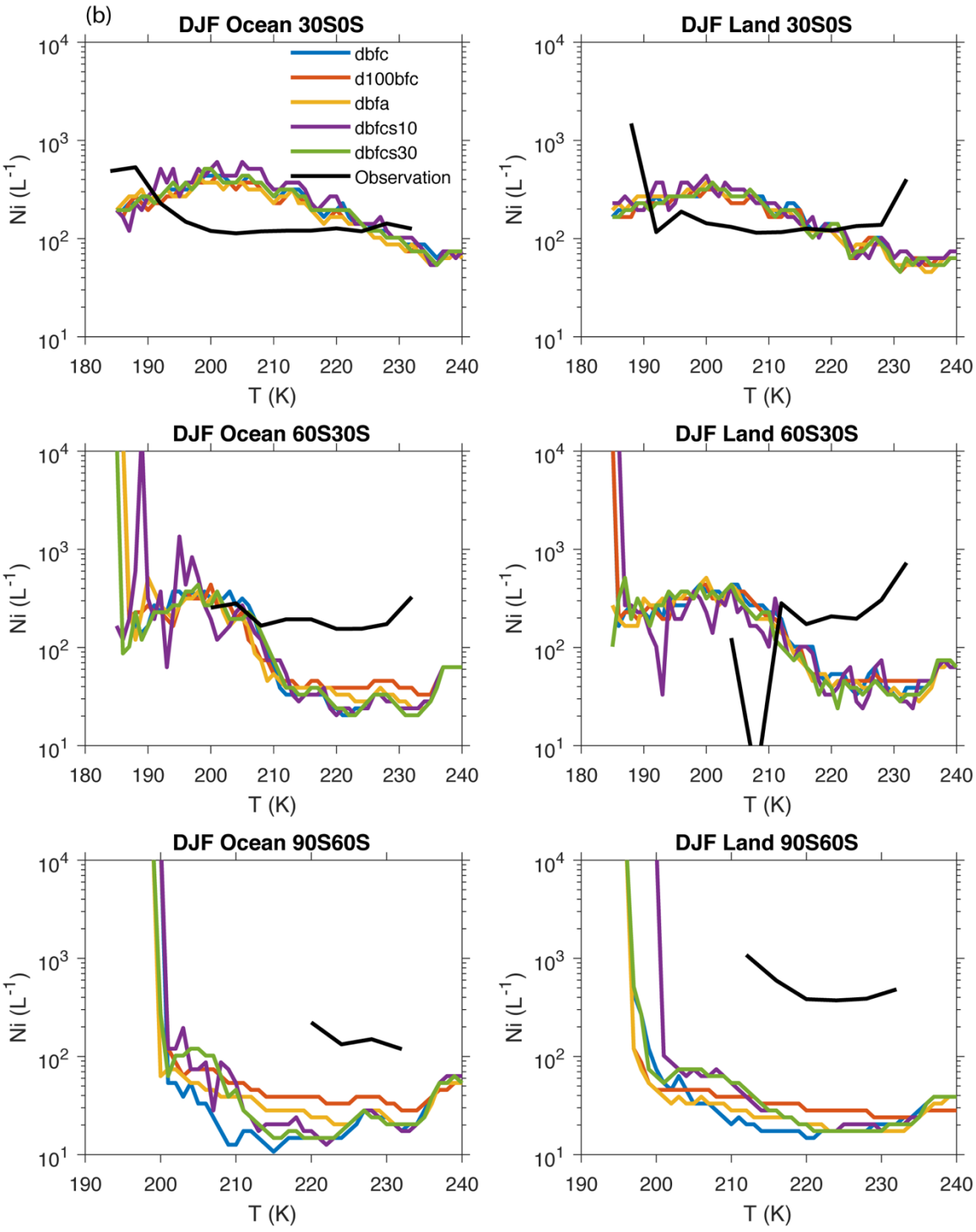

Figure S8. Median in-cloud ice number concentrations for JJA in the Southern Hemisphere from the $N(D)_1$=0 assumption for CALIPSO observations summarized by Mitchell et al. (2018) together with the median predicted ice number concentrations from a set of the simulations described in Table 1. The modeled cloud optical depth is restricted to the range from 0.3 to 3.0. (b) as in (a) but for DJF in the Southern Hemisphere.

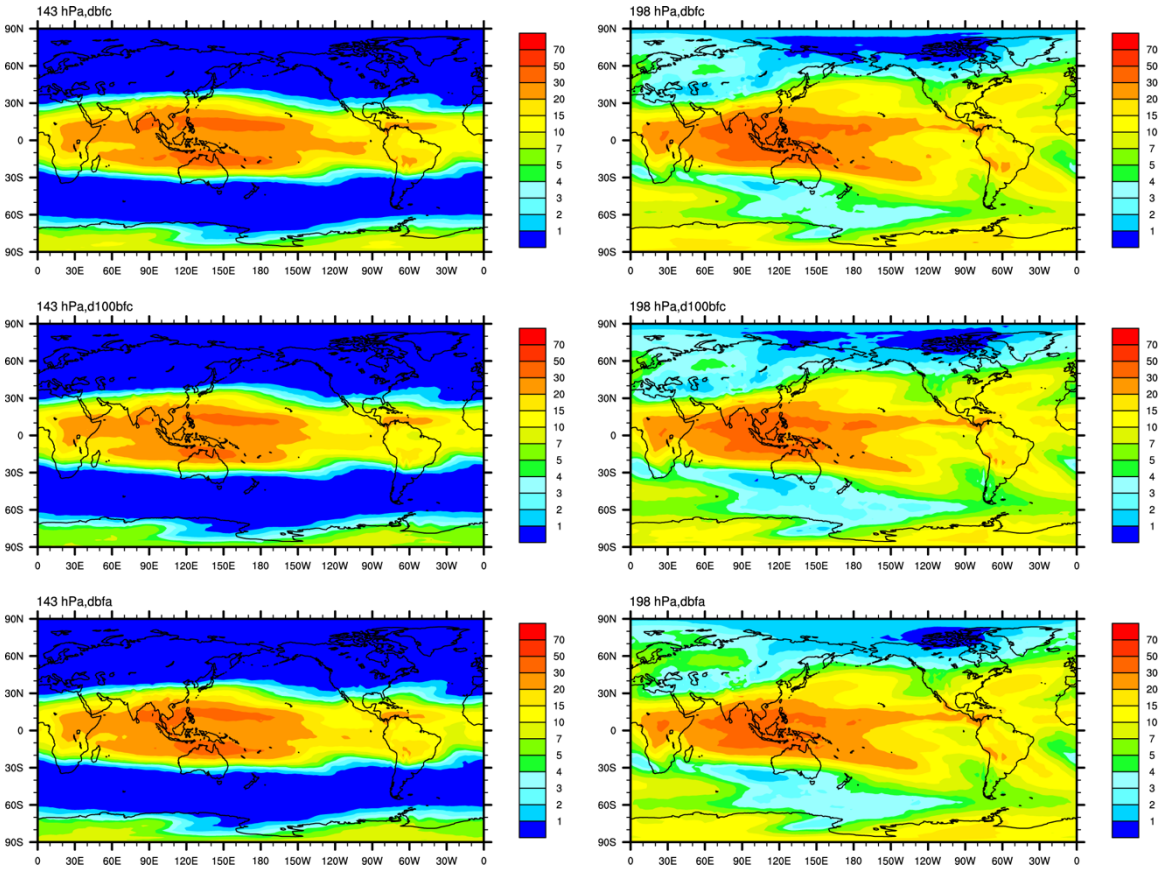

Figure S9. Annual average frequency of occurrence of ice supersaturation at 143 hPa (left panels) and 198 hPa (right panels). The dbfc, d100bfc, and dbfa simulations are shown for the top, middle, and lower panels, respectively.

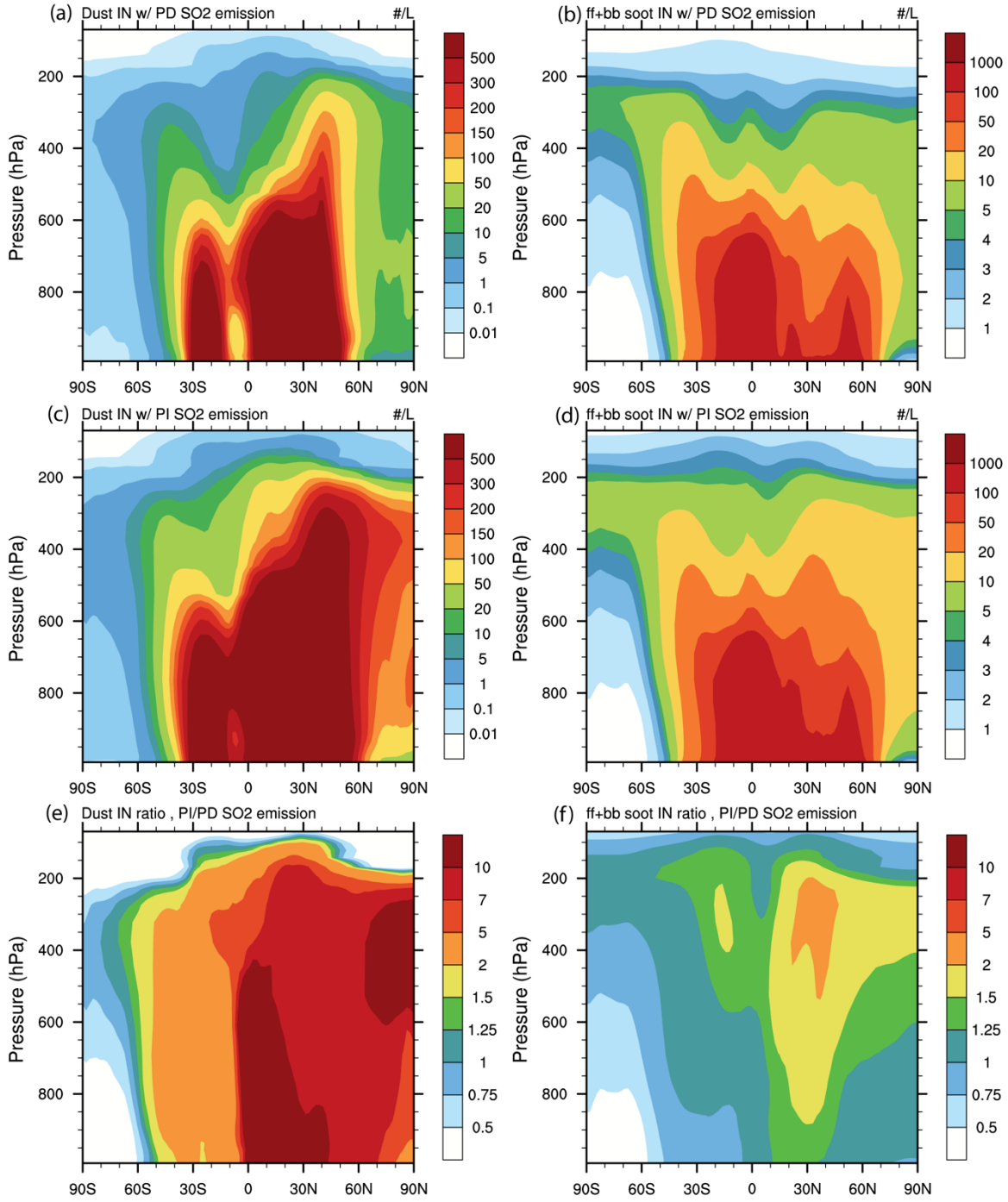

Figure S10. (a) Concentration of dust acting as an INP (L^{-1}) when using present day (PD) SO_2 emissions. (b) Concentration of fossil fuel and biomass burning soot acting as an INP (L^{-1}) when using PD SO_2 emissions. (c) Concentration of dust acting as an INP (L^{-1}) when using pre-industrial (PI) SO_2 emissions. (d) Concentration of fossil fuel and biomass burning soot acting as an INP (L^{-1}) when using PI SO_2 emissions. (e) Ratio of dust INP concentrations from using PI and PD SO_2

emissions. (f) Ratio of fossil and biomass burning INP concentrations from using PI and PD SO_2 emissions.

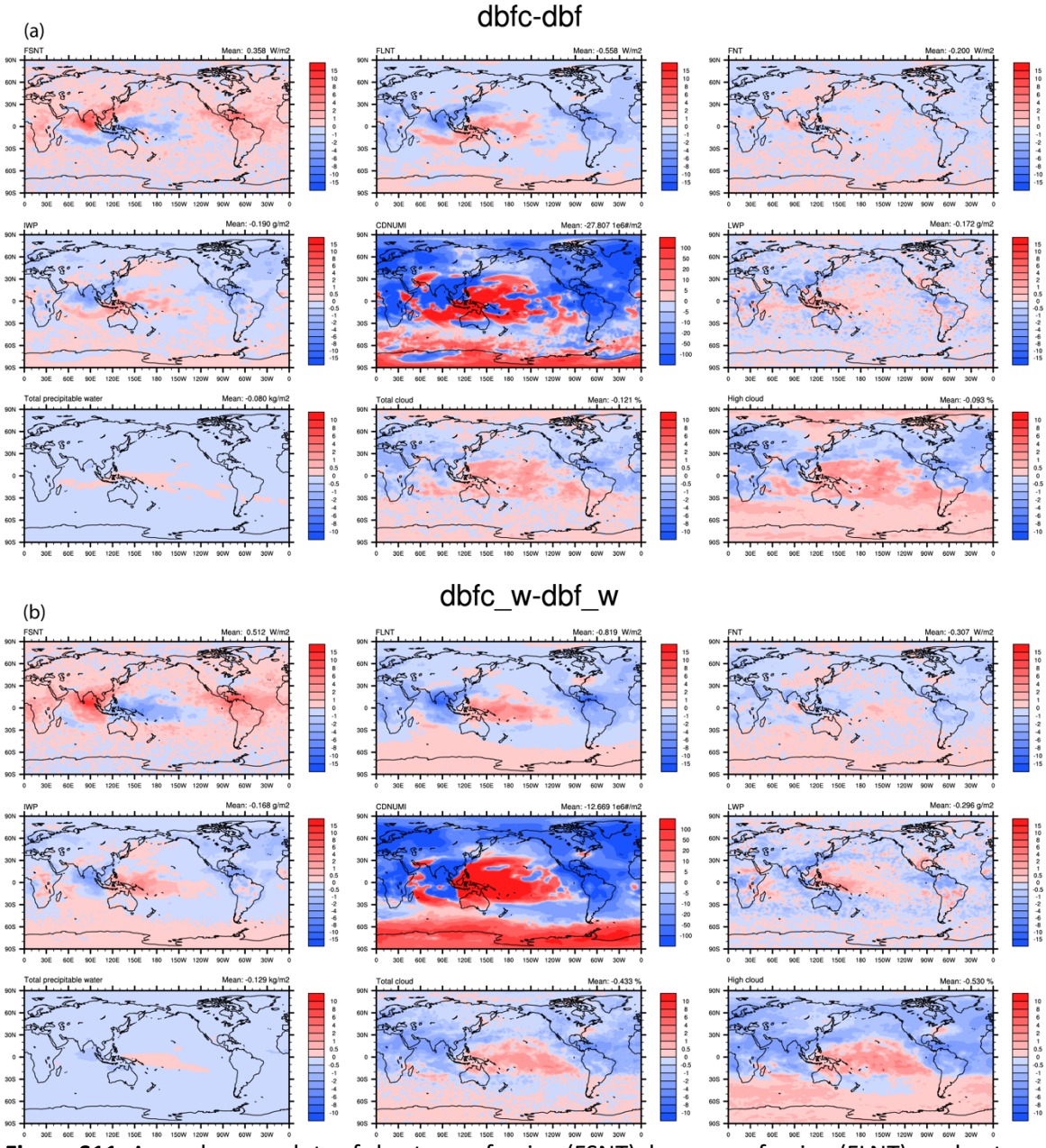

Figure S11. Annual mean plots of shortwave forcing (FSNT), longwave forcing (FLNT), and net forcing (FNT), as well as the change in the vertically integrated ice water path (IWP), total precipitable water, total cloud fraction and high cloud fraction for the difference between the dbfc and dbf simulations (a) and the dbfc_w and dbf_w simulations (b).

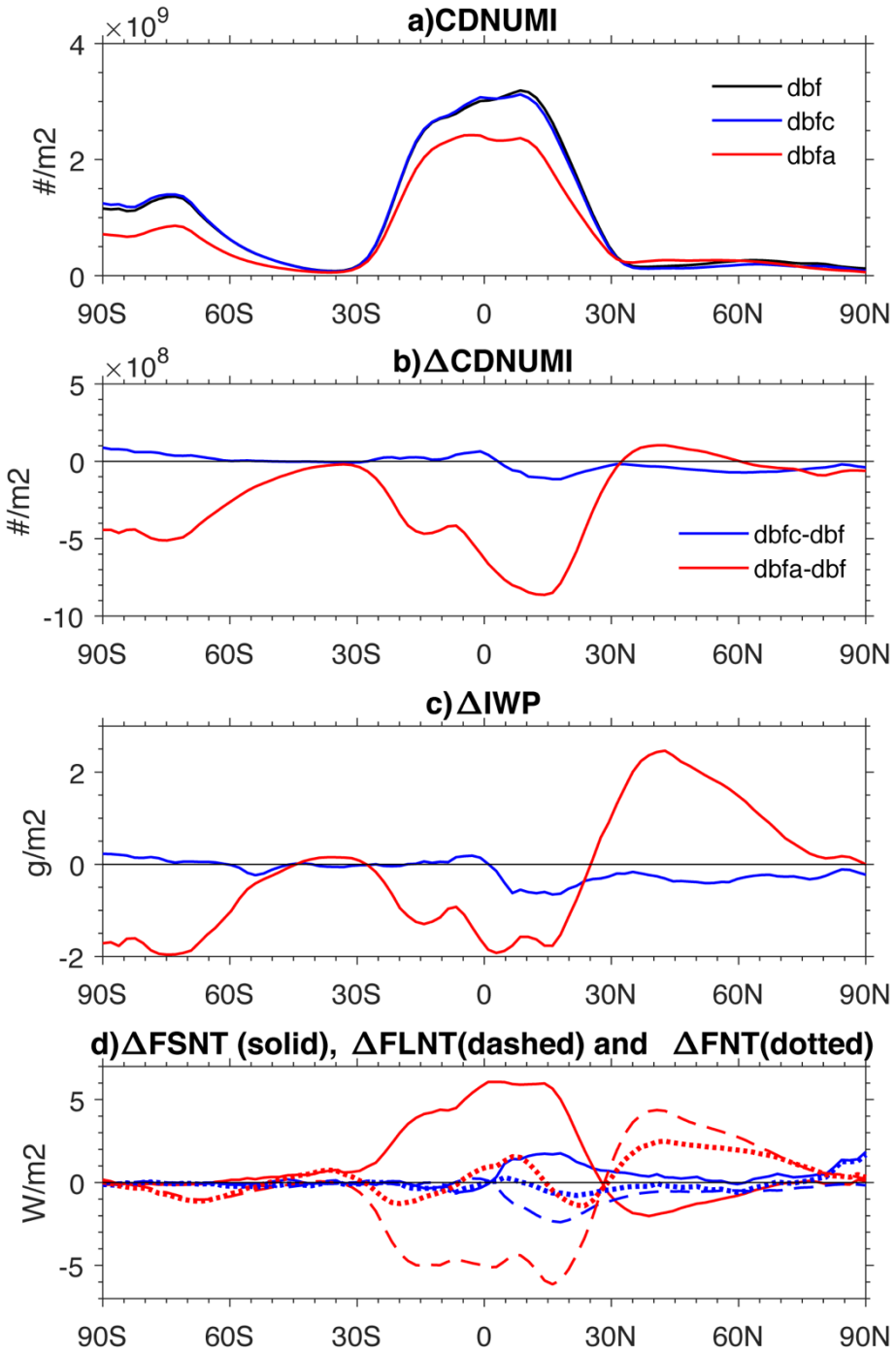

Figure S12. (a) Annually averaged vertically integrated grid box average ice number concentration, (b) Change in vertically integrated ice number concentration between the dbfc and dbf simulations and between dbfa and dbf simulations, (c) change in ice water path between dbfc and dbf and between dbfa and dbf, (d) change in short wave (ΔFSNT), long wave (ΔFLNT) and net forcing (ΔFNT) for dbfc and dbfa.

Table S1. Variation of integrated ice number concentration in different simulations (10^8 m^{-2})

	WGRID_COMP[1] [Zhou et al., 2016]	wGARY[2] [Zhou et al., 2016]	WTKE_COMP[3] with updraft limited to < 0.2 m/s.	CAM5.1 with updraft limited to < 0.2 m/s [Liu et al., 2012]	Full range WTKE[4] [Zhou et al., 2016]	dbfc_w	dbfc
CDNUMI (10^8 m^{-2})	1.19	4.51	10.3	4.82	44.6	10.1	12.3

[1]Case WGRID_COMP used the IMPACT model together with the grid-based updraft with the water vapor accommodation coefficient α=0.1

[2]Case wGARY used the same model set-up as WGRID_COMP but used updrafts based on Gary (2006; 2008)

[3] Case WTKE_COMP, used updrafts based on the turbulent kinetic energy (TKE), but limited to < 0.2 m s^{-1}. The integrated ice number concentration is approximately twice the value (4.82×10^8 m^{-2}) reported by Liu et al. (2012) which used the same set-up but a smaller sulfate number from the CAM5/MAM3 module.

[4]Case WTKE used the full range of updrafts based on TKE.

Table S2. Major emissions used in the model (Tg/yr).

Species	Global	Reference
Fossil/biofuel BC	5.15	CAM5, year 2000 emissions, Lamarque et al. (2010)
Fossil/biofuel OC	17.79	Same as above
Open biomass burning BC	2.61	Same as above
Open biomass burning OC	32.55	Same as above
Anthropogenic SO_2	101.23	Same as above
Aircraft BC	0.0059	Zhou and Penner (2014)
Aircraft OC	0.0064	Zhou and Penner (2014)
Dust	3734.7	This study. Calculated online based on the Zender et al. (2003) dust model.